Gallacher BJ, Burdess JS, Hu ZX, Grigg HT, Dale C, Hedley J, Fu C, Spoors J, O'Meara N, Keegan N. Experimental verification of a quasi-trapped degenerate mode magnetic acoustic resonator. *Sensors and Actuators A: Physical* 2018, 269, 238-248.

Experimental Verification of a Quasi-Trapped Degenerate Mode Magnetic Acoustic Resonator

by

B. J. Gallacher[a], J.S. Burdess[a], Z.X. Hu[a], H.T. Grigg[a], C. Dale[a], J Hedley[a], C Fu[a], J Spoors[a], N O'Meara[b] and N Keegan[a]

[a] *Newcastle University, Newcastle, NE17RU, UK*

[b] *Polytec Ltd, Lambda House, Batford Mill, Harpenden, AL5 5BZ, UK*

1.0 Introduction and Motivation

Trapped and quasi-trapped mode resonators have a long history [1-3] and have formed the basis for two hugely successful technologies. High frequency crystal filters often operate in a trapped shear mode configuration in order to exploit the high intrinsic mechanical quality factor and high stability. Similarly, the Quartz Crystal Microbalance (QCM) also operates in a trapped shear configuration for the same reasons. Thus far there is no evidence in the literature of degenerate trapped or quasi-trapped shear mode resonators. They offer significant advantages in mass sensing applications and offer alternative designs for Coriolis gyroscopes.

In the case of Coriolis gyroscopes, modal degeneracy between the driven and sensed modes of vibration results in a resonant response to the applied input rate. With Quality factors typically of the order of 10^4 for conventional MEMS gyroscopes, the benefits of degeneracy are an increase in rate sensitivity by several orders of magnitude over non degenerate designs [4]. In addition, the degeneracy between the modes permits reduced excitation levels of the driven mode thus reducing the signal noise stemming from the drive signal by a factor equal to the Quality-factor of the degenerate mode pair.

Mass sensing using the absolute frequency shift of a single mode of vibration of a resonator, [5,6], is susceptible to environmental effects that can cause changes to the resonant frequency of that single mode. An alternative approach, which is largely insensitive to the unwanted causes of frequency shift, is made possible through using the well-known degenerate modal properties of cyclically symmetric structures [7]. Independent cyclic modes which vary circumferentially as $\sin(n\theta)$ and $\cos(n\theta)$, $n \neq 0$, share a common natural frequency ω_n. When mass is added to these resonators, in a way which disrupts this symmetry, the degeneracy is broken and the single natural frequency 'splits' to yield two, close, natural frequencies ω_{n1} and ω_{n2}. This frequency split is used to determine the added mass. Common mode effects e.g. temperature and liquid effects are removed by this differential measurement [8, 9]. Previous work [10] demonstrated that degenerate mode sensing offered a factor of around 70 improvement in resolution for degenerate mode sensing compared with an absolute frequency measurement.

Mass sensing under liquid presents a significant challenge to mechanical resonators. It has been reported, [5], that out of plane surface displacement causes severe damping rendering resonant based mass detection impossible. In this study the objective is to configure the resonator geometry to support **highly localised, degenerate** modes with dominant in-surface shear vibrations at its surface. The study will include characterisation of the surface displacements

to compare the relative size of the in-plane and out of plane displacements. The resonator will be expected to possess an inherently high quality factor due to the localisation of the vibration and permit mass detection under liquid through differential measurement of a pair degenerate resonant frequencies [8]. The localisation investigated in this study results in trapping of the in-plane displacements components.

2.0 Description of the System

An analysis of the antisymmetric SH wave dispersion characteristics of time-harmonic waves in elastic waveguides, as described in [11], illustrates how highly spatially localised resonant responses can result from the appropriate choice of geometry. The highly localised resonant responses can be characterised either as pertaining to "trapped" modes or "quasi-trapped" modes of the elastic structure. In trapped modes all components of the displacement field are highly localised and thus the energy associated with the resonance is conserved or "trapped". In contrast, quasi-trapped modes do radiate energy as one component of the displacement field is not localised. Figure 1 shows the structure of such a plate. Localisation, including both quasi-trapping, of antisymmetric thickness shear waves is made possible due to surface loading on the plate caused by the mesa. The mesa is circular to maintain axisymmetry but this is not essential for localisation. In the case considered the mesa and the plate are made from identical materials. Piezoelectric actuation using single crystal plates is commonplace in high frequency filtering and QCMs. However, the anisotropic elasticity of the piezoelectric crystals would break the axisymmetry of the design required for degenerate resonant responses. Magnetic acoustic coupling provides an alternative excitation method which permits the use of elastically isotropic material thus maintaining the desired degeneracy [12-17]. The material must however be electrically conductive to support the generation of eddy currents essential for excitation via this method. The material was chosen to be aluminium due to its high electrical conductivity. Figure 2 illustrates the aluminium plate, mesa and the permanent magnet configuration used to electromagnetically excite the plate into resonance.

Referring to the dispersion relations reported in the literature [11], the dispersion relation for an infinite aluminium plate can be plotted for the two thicknesses corresponding to the plate with and without the mesa. Figure 3 shows the dispersion plots. The Bechmann numbers k_{B1} and k_{B2} define the frequencies in the plate and mesa respectively corresponding to case where the radial wave number ξ of the antisymmetric SH wave is zero [1, 2]. Furthermore, the Bechmann numbers define the cut-off frequencies below which the radial wave number ξ of the antisymmetric SH wave becomes imaginary. By selecting a frequency parameter k_n such that $k_{B1} < k_n < k_{B2}$ the antisymmetric SH wave in the region defined by the mesa will be propagating whilst the antisymmetric SH wave outside the mesa will be evanescent. The mode is localised. The natural frequency ω_n is related to the frequency parameter by k_n by

$$k_n{}^2 = \omega_n{}^2 h^2 \frac{\rho}{\mu}$$

where ρ and μ are the mass density and shear modulus for the aluminium.

For the perfectly axisymmetric case the cyclic modes of order *n* are degenerate and share the same the natural frequency ω_n. The degenerate modeshapes are rotated relative to each other by $\pi/2n$ however their absolute orientation is indeterminate. The trapped and quasi-trapped modes are expected to have a natural frequency ω_n with $\omega_{B1} < \omega_n < \omega_{B2}$ where ω_{B1} and ω_{B2} are the cutoff frequencies corresponding to k_{B1} and k_{B1}, respectively. The degenerate mode pair will therefore be trapped or quasi-trapped modes. Structural imperfections break the axial symmetry and cause the degenerate frequency ω_n to split into two close frequencies ω_{n1} and ω_{n2}. The absolute orientation of the split modeshapes is now determinate. The modeshapes corresponding to the natural frequencies ω_{n1} and ω_{n2} will still be trapped or quasi-trapped.

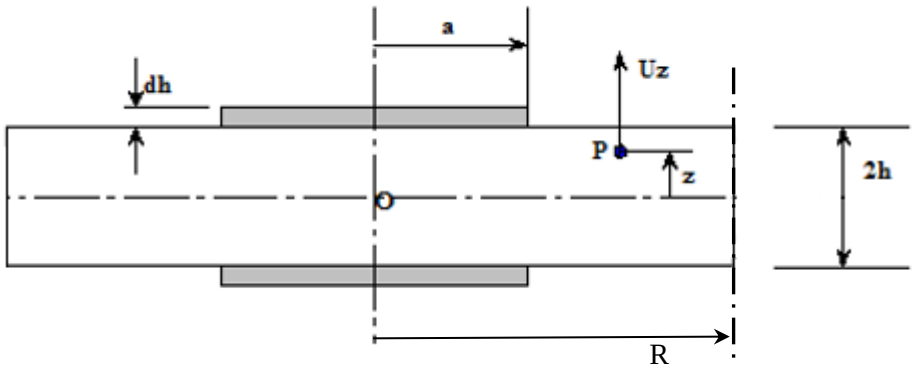

Figure 1. Schematic of the plate and mesa. The radii of the mesa and plate are defined as (a) and (R), respectively. The mesa and plate thicknesses are defined as (dh) and (2h), respectively. The out of plane displacement component of an arbitrary point P within the plate is defined as Uz.

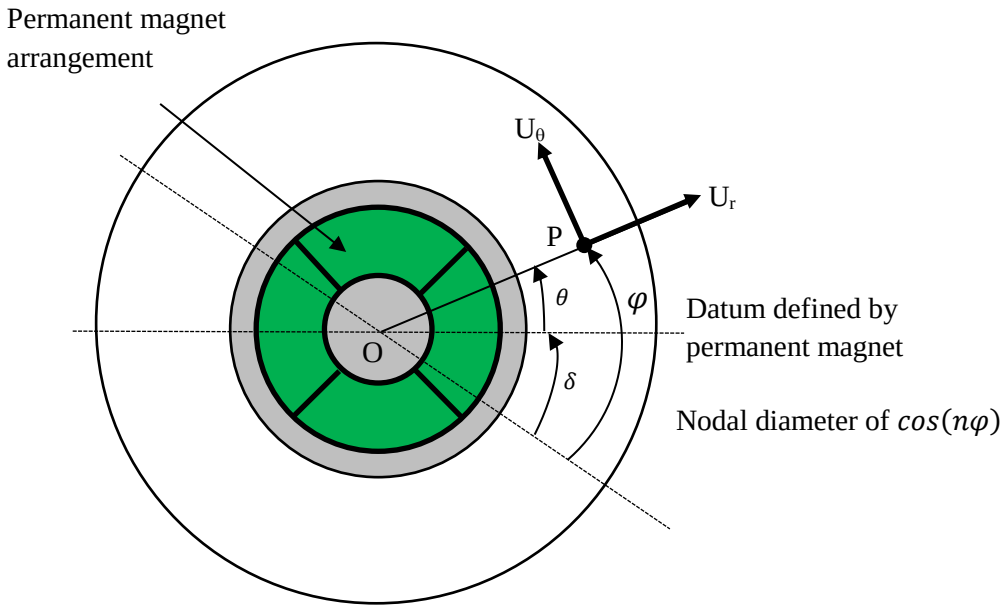

Figure 2. Plate, mesa and permanent magnet configuration. The geometric centre of the plate, mesa and magnet configuration is point O. The angular coordinate θ defines the angular position of the arbitrary point P on the plate with respect to the datum defined by permanent magnet configuration. The orientation of the nodal diameter of the $cos(n\varphi)$ mode with respect to the datum is defined by the angular coordinate δ. The angular coordinate φ defines the angular position of the point P with respect to the nodal diameter. The radial and tangential displacement components of the point P are U_r and U_θ, respectively.

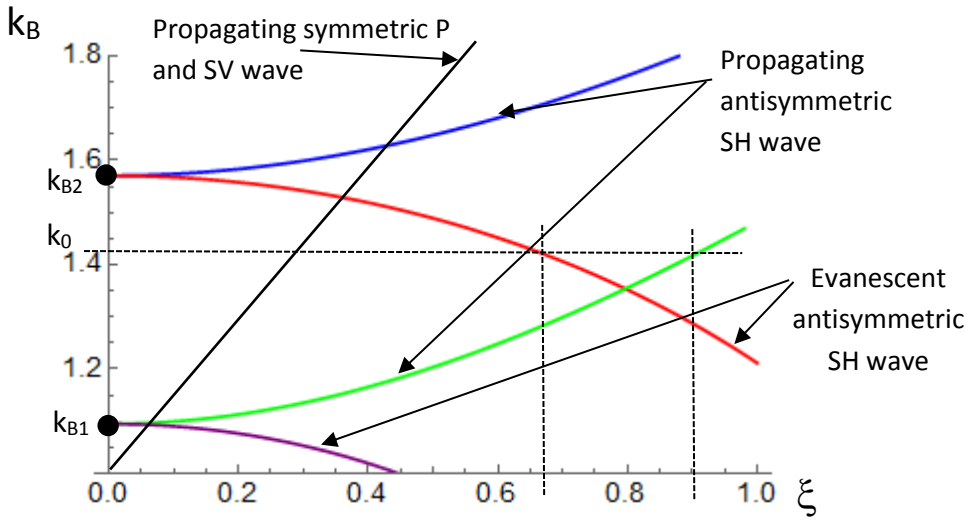

Figure 3. Dispersion plot for layered plate. The parameters k_{B1} and k_{B2} are the Bechmann numbers for the plate and mesa, respectively and define the nondimensional frequencies in the plate and mesa corresponding to case where the radial wave number ξ is zero. The Bechmann numbers define the cutoff frequencies for the SH waves of the structure. The term k_0 defines the nondimensional design frequency and it must located with the cutoff frequencies defined by the Bechmann numbers.

Figure 3 also includes the dispersion relation for the lowest order symmetric P and SV waves. If the boundary conditions permit, the resonant response in the vicinity of ω_n will contain components of symmetric P and SV waves which are always propagating. In this situtation the response will be quasi-trapped.

2.0 Excitation and Detection of the Degenerate In-Plane Shear Modes

2.1 Excitation

Electromagnetic excitation of acoustic waves was first demonstrated in the late 1960's [12] and has been explored in recent years as a means of realising high quality factor resonators for mass detection [13-17]. Figure 4 illustrates the device, the excitation and detection coils. The mechanical resonator is an aluminium plate with a central mesa machined symmetrically on its top and bottom surfaces. A high frequency sinusoidally time varying current is driven through the pancake coil situated below the central mesa. Directly below the excitation pancake coil is a cyclically symmetric arrangement of permanent magnets.

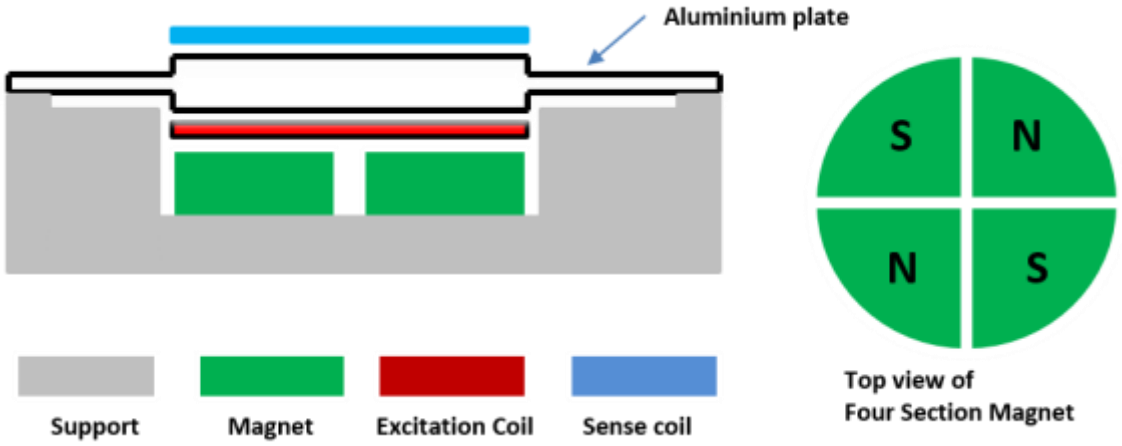

Figure 4. Excitation and detection configuration.

A heuristic view of the excitation method provides a useful insight. As the pancake coil is axisymmetric to first order, the induced eddy current in the aluminium plate will also be axisymmetric. Due to its frequency the eddy current is confined within the skin depth near the bottom surface of the aluminium plate. The Lorentz interaction of this eddy current with the permanent magnetic arrangement results in a circumferentially distributed time varying force that can be used for resonant excitation of degenerate modes. The nature of the forcing from the combination of static and time varying magnetic fields is conveniently described by the Maxwell stress [18].

With reference to Figure 1 and Figure 2, $(\underline{\hat{r}}, \underline{\hat{\theta}}, \underline{\hat{z}})$ defines unit vectors in the radial, tangential, and out of plane directions. The displacement vector of an arbitrary point P is $\left(U_r\underline{\hat{r}}, U_\theta\underline{\hat{\theta}}, U_z\underline{\hat{z}}\right)$. The air gap between the aluminium plate is very small compared to the in-plane dimensions of

the plate. As a result, the cyclic arrangement of permanent magnets creates a magnetic flux density in the aluminium plate which may be approximated to

$$\underline{B}^{(p)} = B_z^{(p)} \cos(n\theta)\, \underline{\hat{z}}\,.$$

For the case considered *n*=2. Fourier decomposition of the cyclic arrangement of permanent magnets will also contain other harmonics. These additional harmonics are small relative to the fundamental component *n=2* and are consequently neglected.

The magnetic flux density generated by the pancake coil can be described by

$$\underline{B}^{(c)} = \left(\tilde{B}_r^{(c)} \underline{\hat{r}} + \tilde{B}_z^{(c)} \underline{\hat{z}}\right) e^{i\omega t}$$

The magnetic flux density of the coil is orders of magnitude smaller than that of the permanent magnetic. A small parameter ϵ may then be defined as

$$\epsilon = \frac{\tilde{B}_r^{(c)}}{B_z^{(p)}} \text{ where } \epsilon \ll 1.$$

Since the radial component of the field from the coil dominates $\tilde{B}_z^{(c)} \ll \tilde{B}_r^{(c)}$ then the approximation

$$\underline{B}^{(c)} = \left(\epsilon B_r^{(c)} \underline{\hat{r}} + \epsilon^2 B_z^{(c)} \underline{\hat{z}}\right) e^{i\omega t} \text{ can be made.}$$

The total magnetic flux density is therefore

$$\underline{B} = \underline{B}^{(c)} + \underline{B}^{(p)}$$

The Maxwell stress components are due to the total magnetic flux density and are determined from

$$\sigma_{ij} = \frac{1}{\mu_0}\left(B_i B_j - \frac{1}{2}\delta_{ij} B^2\right).$$

The stress component produced within the plate that will excite SH waves is thus given by

$$\sigma_{rz} = \frac{1}{\mu_0}\left(\epsilon B_r^{(c)} B_z^{(p)} \cos(n\theta) e^{i\omega t} + O(\epsilon^3)\right) \quad (1)$$

As the σ_{rz} stress distribution is confined to the within skin depth, the harmonic forcing will preferentially excite in-plane shear modes. Due to the single sidedness of the stress distribution it will be realised that the arrangement will excite both symmetric and skew symmetric shear waves.

2.2 The Effect of Structural Imperfections on Degeneracy

For the perfectly axisymmetric case the cyclic modes are degenerate. The degenerate modeshapes have indeterminate orientation and share the same the natural frequency ω_n. Small structural imperfections, either mass or stiffness, can be treated as perturbations and cause the degenerate natural frequency ω_n to split into two close natural frequencies ω_{n1} and ω_{n2}. The orientation of the modeshapes corresponding to the natural frequencies ω_{n1} and ω_{n2} are fixed within the plate and are determined by the distribution of the structural imperfections. The angular position of the modeshapes may be referred relative to an angular datum defined by the permanent magnet arrangement.

As shown in figure (2), $\theta = \varphi - \delta$ (2)

where δ defines the angular offset between the angular datum and the nodal diameter of the *n*th order cosine mode.

The stress generated by the permanent magnet arrangement of cyclic order *n* can be conveniently described by equation (3)

$$\sigma_{rz} = \frac{1}{\mu_0}\left(\epsilon B_r^{(c)} B_z^{(p)} e^{i\omega t}(\cos(n\varphi)\cos(n\delta) + \sin(n\varphi)\sin(n\delta)) + O(\epsilon^3)\right) \quad (3)$$

Equation (3) shows that structural imperfections which break the perfect degeneracy cause the orientation of the nth order mode pair to be fixed within the plate. The angular offset δ results in force coupling between the pair of *n*th order normal modes. Resonant excitation of the *nth* order modes can be achieved by adjusting the excitation frequency of the coil such that $\omega \cong \omega_n$. The cyclic order *n* of the resonant vibration can be determined by rotating the permanent magnet arrangement relative to the modal diameter such that δ is varied. The radial distribution of the forcing generated by the Maxwell stress described by equation (3) will in general excite all *n* order mode pairs when the excitation frequency coincides with one of the resonant values. The radial order can be determined from the relative position of the modal response in the frequency response spectrum.

2.3 Frequency Response

Small structural imperfections cause the degenerate natural frequency ω_n of the perfectly axisymmetric case to split into two close natural frequencies ω_{n1} and ω_{n2}. When the excitation frequency of the time harmonic external excitation is adjusted to coincide with either of the two *nth* order natural frequencies ω_{n1} or ω_{n2}, the magnitude of the frequency responses of the two modes described by modal coordinates q_1 and q_2 are given by [19]

$$|q_1|^2 = (\mu_1 Q_1)^2 \left|\cos\left(n\delta + \frac{1}{2}\alpha_1\right)\right|^2 + \gamma_1 = \frac{1}{2}(\mu_1 Q_1)^2\left(1 + cos(2n\delta + \alpha_1)\right) + \gamma_1$$

$$|q_2|^2 = (\mu_2 Q_2)^2 \left|\sin\left(n\delta + \frac{1}{2}\alpha_2\right)\right|^2 + \gamma_2 = \frac{1}{2}(\mu_2 Q_2)^2\left(1 - cos(2n\delta + \alpha_2)\right) + \gamma_2$$

(4)

Q_n is the quality factors of the modes q_n . The term μ_n represents the scaling factor associated with the magnetic circuit configuration. The term γ_n is the non-resonance contribution made to each of the frequency responses. The dynamics of the slightly imperfect plate may be described purely in terms of the idealised $\sin(n\theta)$ and $\cos(n\theta)$ modeshapes for a single value of *n* when $\alpha_2 - \alpha_1 = 0$. In this case equation (4) shows that the angular offset δ governs the response magnitudes of the pair of *n*th order modes and the relative phase between the responses is $\frac{\pi}{2}$. By measuring the response magnitudes of a pair of modes at several values of δ the cyclic order *n* of the pair can be determined. This provides a route for experimental verification of the mode order in the absence of direct measurement of the modeshape e.g. via laser vibrometry.

2.4 Detection

The detection arrangement is shown in Figure 5. Two sense coils, labelled *S1* and *S2*, are used for detection of the vibratory motion. The EMF generated in the aluminium plate is a consequence of two effects. The time dependent vector potential $\underline{A} = A_\theta(r,z)e^{i\omega t}\underline{\hat{\theta}}$ generated by the excitation coil generates an EMF in the aluminium plate which is independent of the vibration. The vibration of the plate in the total magnetic field from the excitation coil and permanent magnets produces the EMF *V* described by

$$V = -\oint \frac{d\underline{A}}{dt}.\underline{dl} + \oint\left(\underline{v}\ x\ \underline{B}\right).\underline{dl} \tag{5}$$

Equation (5) describes the total EMF in the plate. Detection of the motional EMF exploits the different variations in fields $\underline{A}$ and $\underline{B}$ in the vicinity of two identical sense coils *S1* and *S2*. Since the separation between the sense coils is small relative to the mean distance from the excitation coil then $\underline{A}$ is approximately constant at the sense coils. The $\underline{B}$ field, which is produced by the permanent magnet and the excitation coil, varies significantly across the sense coils. The EMF induced by the vibration in the sense coils *S1* and *S2* is *V1* and *V2*, respectively. Performing a differential measurement of the EMFs *V1* and *V2* produced in the two sense coils therefore removes the contribution from the excitation coil. For the modes of interest the radial displacement is antisymmetric through the thickness of plate. In this case the differential measurement of the EMF $V_1 - V_2$, produced by the pair of sense coils yields a signal proportional to the resultant radial displacement u_r and its interaction with the z component of the permanent magnetic field $B_z^{(p)}$and is described by

$$V_1 - V_2 = \alpha u_r(z)B_z^{(p)}(z)e^{i\omega t} \tag{6}$$

The parameter α is determined by the geometry of the configuration and the quality factor for resonant excitation. The contribution to the EMF $V_1 - V_2$ from the time dependent vector potential $\underline{A}$ produced by the excitation coil is removed by the differential measurement. This is advantageous when detecting the antisymmetric modes as it excludes symmetric modes.

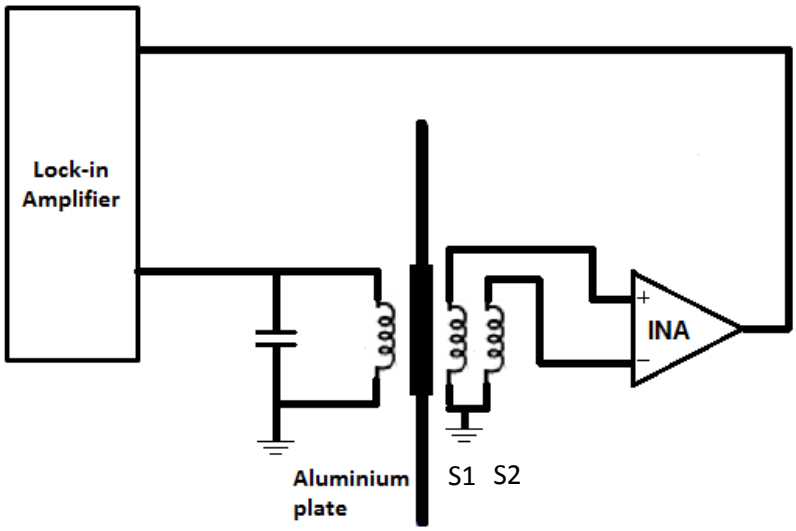

Figure 5. Differential sensing setup. The pair of identical sensing coils S1 and S2 enable differential sensing of the motional EMF when used in conjunction with the instrumentation amplfier (INA)

3.0 Finite Element Modal Analysis

A full elastic model of the experimental device was developed using ANSYS finite element software. With reference to Figure 6, the dimensions were set to a = 10 mm, h = 0.97 mm, and dh= 0.195 mm, corresponding to the aluminium plate under experimental investigation. The outer diameter of the plate was set equal to 45 mm. The step size is approximately 10% of the plate thickness and represents a large step. This size of step was chosen in order to produce parasitic out of plane displacements to enable the use of conventional laser Doppler vibrometry. It was expected that a step of this magnitude would cause coupling between the SH, SV and P waves at the vertical edge of the step [11]. With reference to Figure 2, the symmetric SV and P waves will be propagating. The out of plane displacement is expected not to be localised.

A 2D modal analysis using a harmonic element PLANE83 was performed over a frequency range defined by the Bechmann numbers. The circumferential order for modal analysis was set equal to 2. All modes extracted from the modal analysis correspond to degenerate pairs with circumferential distributions in the form $\sin(n\theta)$ or $\cos(n\theta)$ with n=2. The circumferential mode order n can be specified to be any positive integer within the element properties of the finite element code. The case n=2 corresponds to the lowest value of n resulting in useful modal degeneracy. Degeneracy still applies to all cases for n>2. The natural frequency increases with increasing values of n and this may have implications on the electromagnetic circuitry used in the detection scheme.

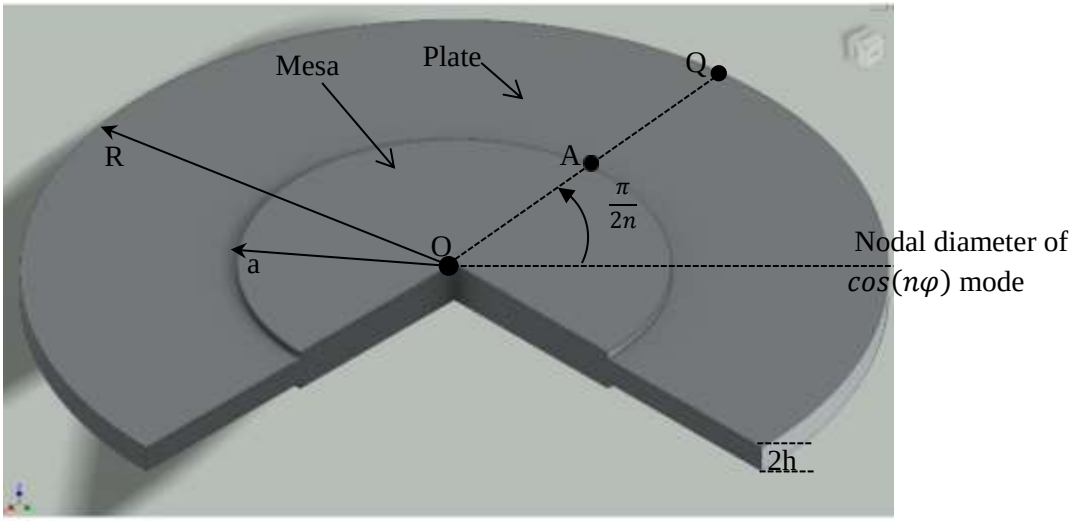

Figure 6. Geometry for finite element analyis. The circumferential order of the harmonic element was set to n=2 as in the experimental configuration. The displacement components U_r, U_θ and U_z along the line OQ was extracted for z=h.

3.1 Finite Element Modeshape and Natural Frequency

Figure 7 shows modeshape of the lowest frequency quasi-trapped mode calculated by finite element analysis. The line plot shows the radial (U_r), tangential (U_θ) and out of plane (U_z) displacements from the origin of the mesa to the outer edge of the plate. The line plot is rotated by $\frac{\pi}{4n}$ relative to the angular datum defining the modeshapes within the finite element model such that the all three displacements components can be compared. The natural frequency of 699.7 kHz was predicted by the finite element model. Using the integral equation method of solution reported in [20] yields a natural frequency of 709 kHz. The agreement between the finite element and integral equation method is 1.5%.

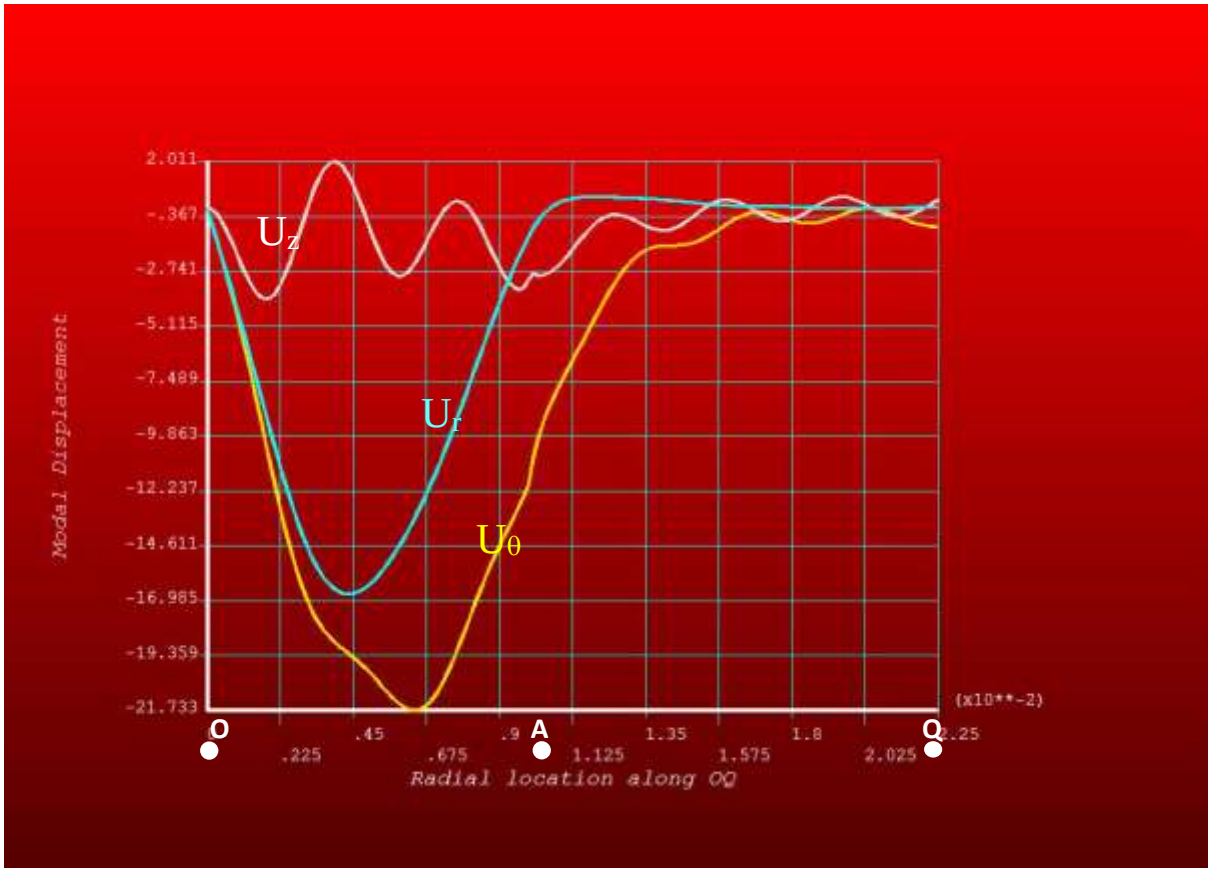

Figure 7. Radial, tangential and out of plane displacement components of the FE determined modes. The displacements components U_r, U_θ and U_z have been plotted along the radial line OAQ. Point A is located on the edge of the mesa. The angular coordinate of the line OAQ defined in figure 3, with respect to the nodal diameter of the $cos(n\varphi)$ mode is specified to be $\frac{\pi}{2n}$.

The finite element model shows that in-plane surface displacements are highly localised to the region defined by the mesa. This is indicative of energy trapping. However, the in-plane displacments components do extend to the outer boundary albeit with reduced amplitude. Both the radial and tangential displacement components are without any nodal circles. Therefore the response corresponds to the *n=2* modes of the lowest frequency. The out of plane displacement does not exhibit the same level localisation for the geometry considered. The out of plane displacement also extends to the outer boundary. Recall that the dispersion relation for the plate shows that the symmetric P and SV waves are always propagaing. The mode is therefore classed as a quasi-trapped mode.

4.0 Experimental Results

One circular aluminium plate of diameter 45 mm was CNC machined to form the prototype device. The tolerance of the CNC milling machine used to make the device is specified to a tolerance of 10 μm. The thickness of the aluminium plate was specified such that the tolerance of the step height relative to the plate thickness was less than 1%. This was in order to minimise deviation of the experimental natural frequency from the design value. At high frequencies the mode density, that is the number of modes in a frequency band, increases significantly. Identification of the desired mode is facilitated by minimising uncertainties on the device dimensions. The thickness of the plate, the radius of the stepped mesa and the outer radius of the plate all influence the natural frequency and the energy trapping of the vibration. An outer diameter of 45 mm was chosen based on the efficacy with which it could be machined via conventional CNC milling. Micromachined versions of the device can be routinely fabricated through standard microfabrication technologies. The device size could readily be reduced to that of the Quartz Crystal Microbalance (QCM). The complete experimental setup is shown in Figure 8. Frequency response tests were performed using a Zurich Instruments HF2LI Lock-in Amplifier, coils and permanent magnet configuration as shown in Figures 4 and 5. The field strength of the permanent magnet supplied from Arnold Magnetic Technologies was 200 mT. A current of 100 mA was supplied to the excitation coil consisting of 16 turns of wire of diameter 100 μm. Modeshape mapping on the surface was performed using a Polytec MSA-100-3D vibrometer. The instrument allows 3D vibration analysis to be performed with picometre resolution of in-plane and out of plane motion.

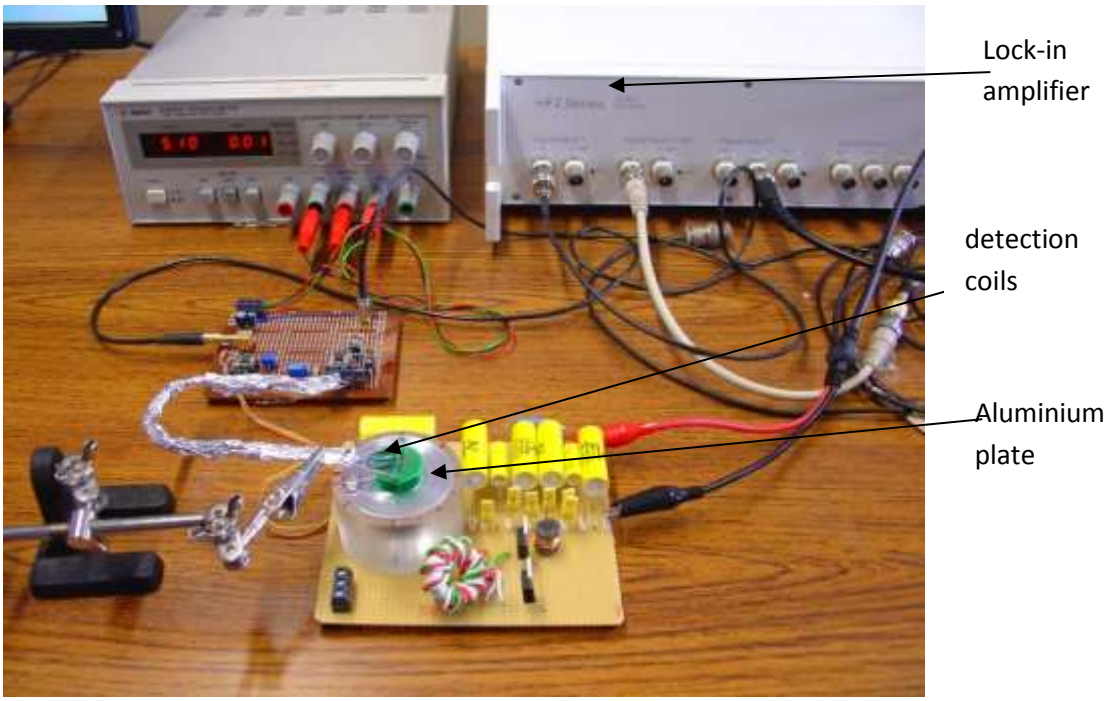

Figure 8. Experimental configuration used to electromagntically measure the modal responses. Excitation and detection coils fabricated onto two separate PCBs. Frequency responses were extracted using the Zurich Instruments HF2 lock-in amplifier.

4.1 Experimental Frequency Response

The frequency response was measured using the differential detection circuitry. The frequency range of interest was determined by the natural frequency calculated from the integral equation method or finite element model. Figure 9 shows the measured frequency response in the vicinity of the predicted natural frequency. The resonant frequencies of the mode pair (Mode 1 and Mode 2) are $\omega_{n1} = 705.644$ kHz and $\omega_{n2} = 705.686$ kHz, respectively corresponding to $\omega_n \cong 705.67$ kHz. The frequency split between the Mode 1 and Mode 2 is 42 Hz, which is 0.006% of ω_n. The Q-factor of the modes is approximately 30000.

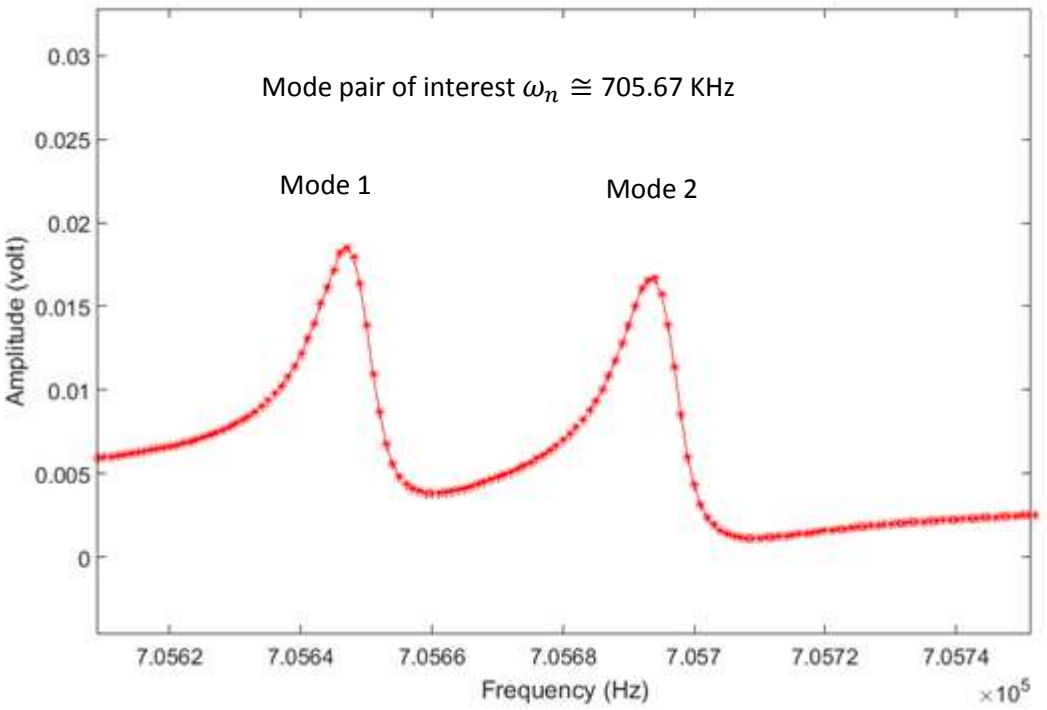

Figure 9. Experimental frequency response. The resonant response of the mode pair is shown as a magnitude plot. Mode 1 and Mode 2 refer to the mode pair which would be perfectly degenerate in the ideal case.

4.2 Determination of the Cyclic Order *n* of the Modes Using the Frequency Response

Equation (4) shows how the magnitude of the frequency response of the pair of modes of cyclic order *n* (Mode 1 and Mode 2) is modulated by the angular offset. The cyclic order *n* may be determined by making frequency response measurements for different values of δ. The frequency responses for the case where $\delta = \frac{p\pi}{8}, p = 0,1,2..8$ are shown in Figure 10. The frequency split between the mode pair $\omega_{n1} - \omega_{n2}$ remains constant whilst the resonant frequencies ω_{n1} and ω_{n2} do shift. This shift in the resonant frequencies may be attributed to thermal effects. Figure 11 shows the maximum magnitude of the two modes of the pair for the different angular locations of the permanent magnet configuration. A nonlinear fitting routine within Mathematica was then used to fit cosinusiodal functions, as described by equation (4), to the data. The fitted terms have the values $\frac{\mu_2 Q_2}{\mu_1 Q_1} = 0.98, \alpha_2 - \alpha_1 = 0.12$. The goodness of the fit for both curves had R^2=0.97, 0.93, for modes q_1, q_2, respectively. Note that $\alpha_2 - \alpha_1 = 0$ when the modeshapes are composed of only one harmonic e.g. *n*=2 in this case. The non-zero relative phase defined by $\alpha_2 - \alpha_1$ suggests other contributions are made to the modeshape corresponding to other harmonics. This is to be expected as the Fourier series decomposition of the magnet configuration will possess other components. The radial order cannot be confirmed using this experimental methodology.

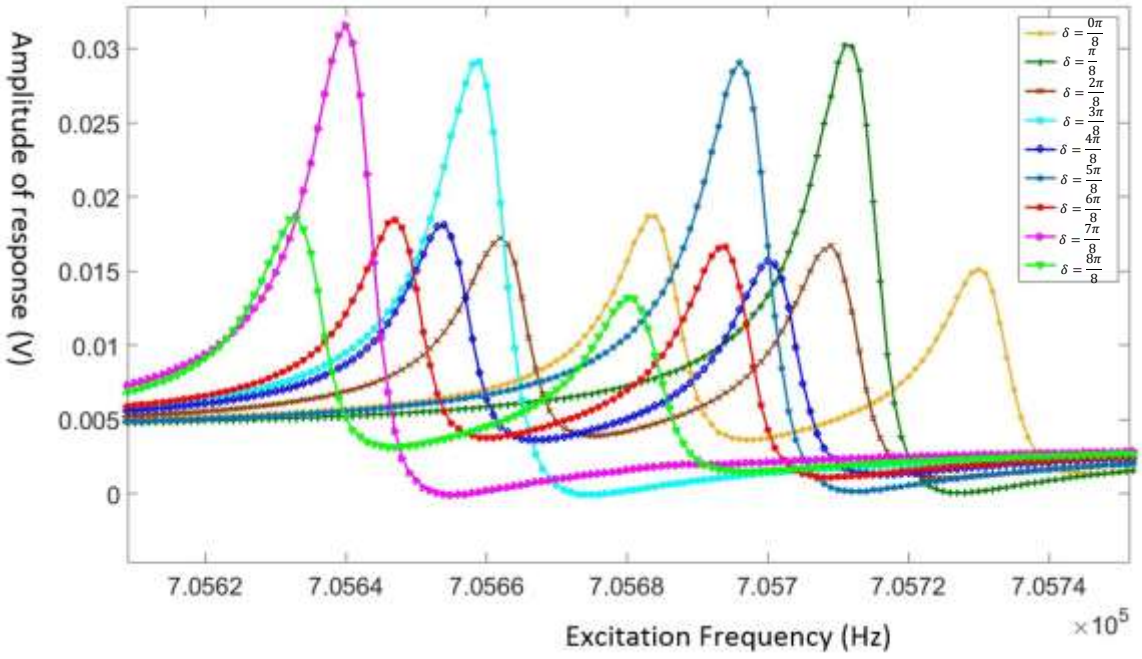

Figure 10. Measured frequency responses for nine angular positions of the magnet configuration. The different angular position $\delta = \frac{p\pi}{8}, p = 0,1,2..8$ are labelled on the figure as data.

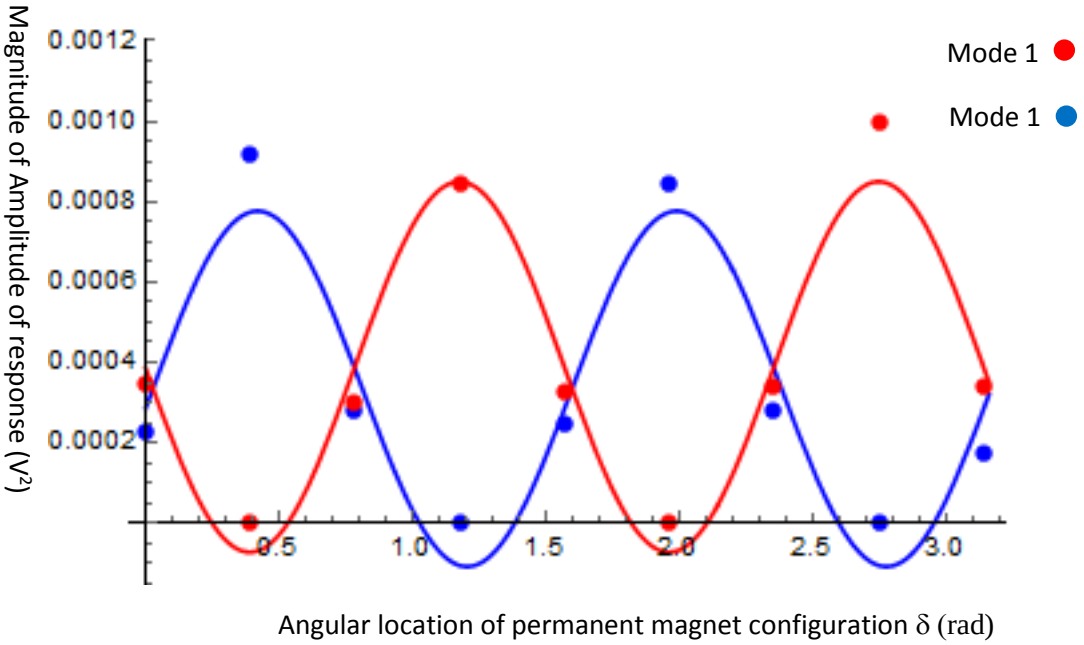

Figure 11. Magnitude of the frequency response for different angles of δ. The angle δ was adjusted by rotating the permanent magnet configuration relative to the aluminium plate.

4.3 Modeshape Mapping using Laser Doppler Vibrometry

A full characterisation of the in-plane displacements components of the modeshape is not possible using the electromagnetic detection circuit. The Polytec MSA-100-3D vibrometer was used to map the surface displacements in rectangular coordinates with the origin located at the centre of the mesa. The radial and tangential displacement components were subsequently obtained by post processing of the data. The area of the mesa was scanned. Figure 12 shows the radial and tangential components of the resonant response with resonant frequency $\omega_{n1} =$ 705.644 kHz. This corresponds to Mode 1. Mode 2 is rotated relative to its partner by $\pi/4$. The cyclic order of the radial and tangential displacements is clearly n=2. Note that the magnitude of the radial displacement has been plotted. The relative phase between the radial and tangential displacement is shown to be $\pi/4$. Both radial and tangential displacements components of this mode are without any nodal circles and are in agreement with the numerical model.

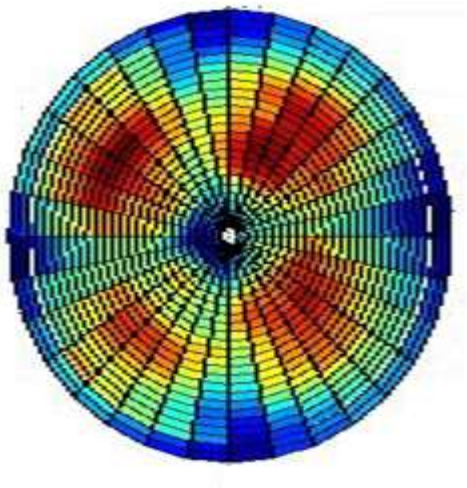

Radial displacement component (U_r) of Mode 1.

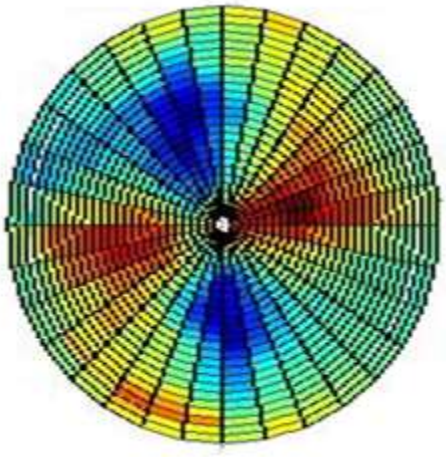

Tangential displacement component (U_θ) of Mode 1.

Figure 12. Radial (U_r) and tangential displacement (U_θ) components of the experimentally determined resonant response of Mode 1. The vibration modeshapes resonance frequencies were measured using the Polytec MSA -100-3D vibrometer. The modeshape data was obtained in Cartesian coordinates before being transformed in polar coordinate

The out of plane displacement component of the modeshape is shown in Figure 13. In contrast with the radial and tangential components, there are three nodal circles within the mesa region. This is in agreement with the finite element results shown in Figure 7. The Fourier series representation of the cyclic arrangement of the permanent magnets will be dominated by the n=2 harmonic. However, the cyclic order n is not clear from the out of plane displacement component of the modeshape. Figure 14 shows the Fast Fourier Transform (FFT) of the measurement displacements in rectangular coordinates for all the measurement points used in the modeshape plots. The ratio of the maximum radial displacement to the maximum out of plane displacement is $\frac{U_r}{U_z} \cong \frac{5}{1}$.

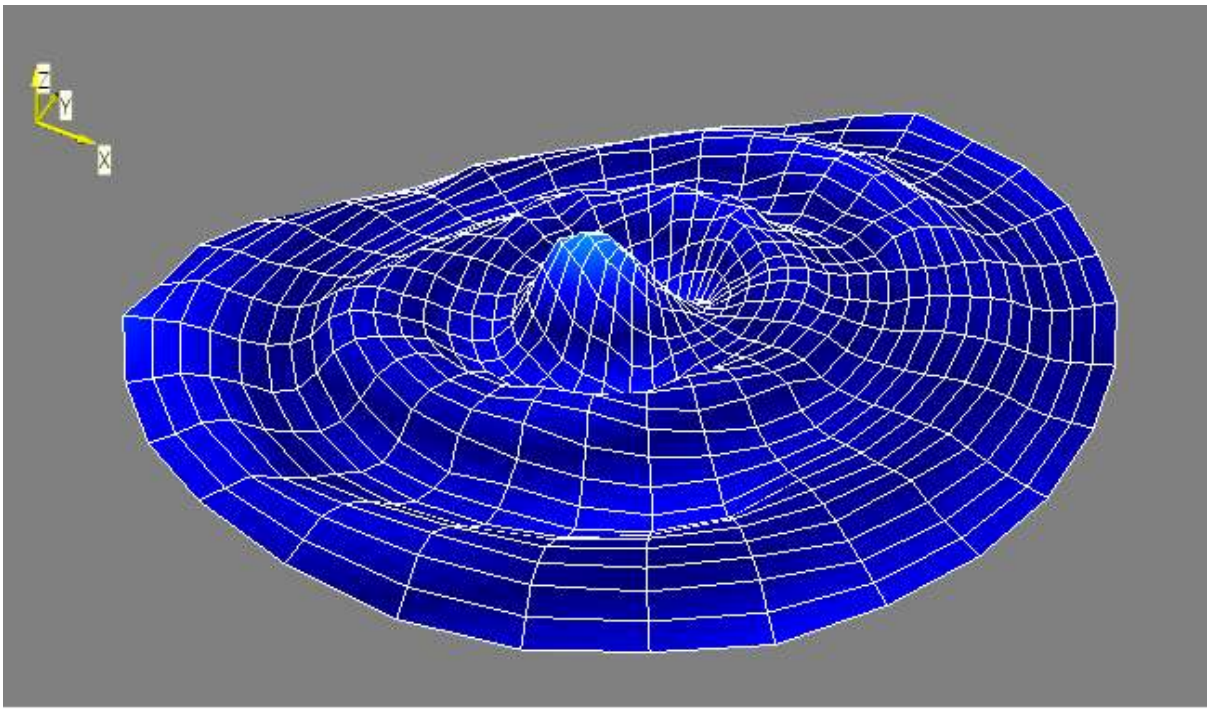

Figure 13. Out of plane displacement component U_z of the experimentally determined resonant response of Mode 1.

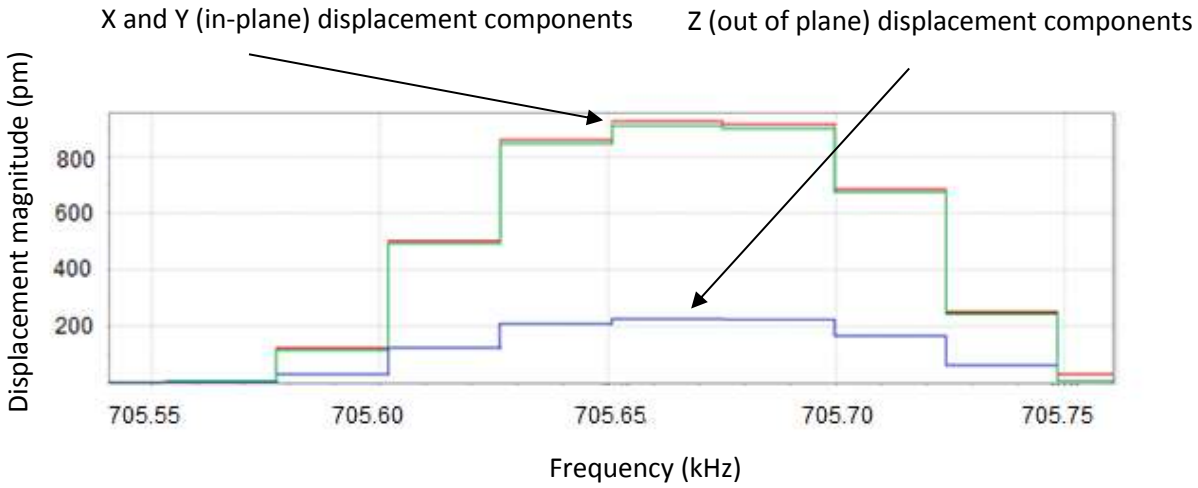

Figure 14. FFT of displacement showing in-plane and out of plane components. The displacements component are in Cartesian coordinates (X,Y,Z) with Z normal to the plane of the aluminium plate and X,Y representing the in-plane rectangular displacements.

4.4 Comparison of Experimental and Modelled Modeshape

The radial and tangential components of the measured modeshape exhibit a dominant n=2 component. Both experimental and numerical results show that the in-plane displacements are without nodal circles and are highly localised to the region defined by the mesa. The maximum out of plane displacement U_z in the experimental and numerical modeshape is significant and

is related to the maximum radial displacement as $\frac{U_r}{U_z} \cong \frac{5}{1}$ and $\frac{U_r}{U_z} \cong \frac{10}{1}$, respectively. All displacement components extend beyond the mesa with localisation more pronounced for the radial and tangential components. Out of plane displacement of the plate surface causes radiative energy loss due to the formation of compressional waves in the surrounding fluid [21]. The edge of the mesa is a contributing factor to the generation of out of plane surface displacement. As described in [22], the discontinuity defined by the vertical edge of the mesa results in a localised region of high in-plane stress acting on the plate. This highly localised shear stress has been shown to contribute to bending of plate and is a cause of out of plane displacement in the plate. A practical method of reducing this well-known edge stress is to remove the geometric discontinuity defined by the vertical step by introducing a fillet. This effectively removes the stress singularity. The introduction of a fillet is readily achievable when using microfabrication techologies through the use of etching, Focused Ion Beam (FIB) or laser melting. For the low cost batch fabricated mass sensor it is envisaged that microfabrication technologies will be employed thus enabling reduction of the edge stress through the formation of a fillet. The dispersion plot shown in Figure 3 shows that the symmetric P and SV waves are always propagating. It is therefore expected that in general the out of plane displacement should extend to the edge of the plate for the geometry considered.

5.0 Conclusions

The circular plate with circular mesa has been shown to possess degenerate modes where the in-plane displacements at the surface are strongly localised to the region defined by the mesa. Outside the mesa the in-plane displacements are attenuated yet are still non-zero at the edge of the plate. In contrast, the out of plane displacement for the geometry considered does not exhibit the same degree of localisation. The location of the resonant frequencies on the dispersion curve suggests that the dominant wave type excited is an antisymmetric SH wave. Symmetric SV and P waves are always propagating and may be generated due to the vertical step forming the mesa.

The modeshapes for the resonant response was determined experimentally using 3D laser vibrometry using the Polytec MSA-100 3D. Electromagnetic detection was also used to establish the resonant frequencies prior to mode mapping on the vibrometer and to confirm the cyclic order of the excited responses. Agreement between the displacement components of the experimental modeshape and the numerical modeshape is remarkable.

Further work will investigate the geometrical parameters required to minimise the amount of out of plane displacement and improve the level of energy trapping. Coriolis gyroscopes never operate within a liquid environment. Therefore, any out of plane displacement in the degenerate modes is not important. Energy trapping of the displacement field of the degenerate modes does offer several advantages for gyroscopic sensors due to the increased quality factor and improved mechanical isolation. In the case of mass sensors where the device must often operate within a liquid environment, reducing the out of plane displacement is desirable as it reduces the compressional waves excited in the surrounding fluid. Mass sensors exploiting flexural

Lamb waves in plates (FPM) have been shown to be operable within a liquid [23]. At the same frequency, the out of plane amplitude of the FPM based mass sensor will be at worst of the same order as the device reported in this work. Most of the vibrational energy will be attributed to the in-plane SH wave therefore improving the performance figure of merit relative to the FPM. The out of plane displacement present in the device reported here is attributed to flexural Lamb waves and can be confirmed from the solution of the Rayleigh-Lamb frequency spectrum for plates [21].

Acknowledgement

This work was funded by the EPSRC under grant EP/K000349/1. The authors also wish to thank the team at Polytec GmbH., Waldbronn, Germany for their assistance in mapping the modeshape using Polytec MSA-100 3D.

References

[1] W. Shockley, D. R. Curran, and D. J. Koneval, Trapped-Energy Modes in Quartz Filter Crystals, The Journal of the Acoustical Society of America 41, 981 (1967); doi: 10.1121/1.1910453

[2] HF. Tiersten, Thickness vibrations of piezoelectric plates. J. Acoust. Soc. Am. 35: 53-58 1963.

[3] B. A. Auld, "Acoustic Fields and Waves in Solids", Vol. 2, Wiley-Interscience, Canada, 1973.

[4] C Acar and A Shkel, "MEMS Vibratory Gyroscopes", Springer, 2009.

[5] K. Lange, et al, Surface acoustic wave biosensors: a review, Anal. Bioanal. Chem. 391,2008, 1509-1519

[6] M. J. Vellekoop, Acoustic wave sensors and their technology, Ultrasonics, 36, 1998, 7-14.

[7] D. L. Thomas, "Dynamics of rotationally periodic structures", *International Journal for Numerical Methods in Engineering*, vol. 14, pp. 81-102, 1979.

[8] A. K. Ismail et-al, The principle of a MEMS circular diaphragm mass sensor, J. of Micromechanics and Microengineering, 16, 2006, 1487-1493

[9] A. K. Ismail et-al, The fabrication, characterization and testing of a MEMS circular diaphragm mass sensor, J. of Micromechanics and Microengineering, 18(2), 2008.

[10] P. Ortiz, R. Burnett, N. Keegan, J. Spoors, J. Hedley, A. Harris, J.S. Burdess, N. Raphoz, J. Collet and C. McNeil, Issues associated with scaling up production of a lab demonstrated MEMS mass sensor, J. Micromech. Microeng. **22** (2012) 115032.

[11] J. D. Achenbach, "Wave Propagation in Elastic Solids", Elsevier (North-Holland), The Netherlands, 1999, pp.1-425.

[12] J.J. Quinn, Electromagnetic generation of acoustic waves and the surface impedance of metals, Physics Letters Vol.25A, No.7, 1967

[13] A.C. Stephenson and C. R. Lowe, Magnetic–acoustic–resonator sensors MARS: a new sensing Methodology**,** Sensors and Actuators A, 72(1), 1998, 32-37.

[14] A.C. Stevenson, B. Araya-Kleinsteuber, R.S. Sethi, H.M. Metha, C.R. Lowe, Biosensors and Bioelectronics 20 (2005) 1298–1304.

[15] M. K. Kang et-al, Energy-Trapping Torsional-Mode Resonators for Liquid Sensing, Proc. 2006 IEEE International Frequency Control Symposium and Exposition, pp. 133-138, Miami, FL, June 2006. DOI: 10.1109/FREQ.2006.275365

[16] Frieder Lucklum, Peter Hauptmann and Nico F de Rooij,Meas. Sci. Technol. **17** (2006) 719–726

[17] F. Lucklum∗, B. Jakoby Sensors and Actuators A 145–146 (2008) 44–51

[18] F.C Moon, Magneto-Solid Mechanics , Wiley, 1984.

[19] S.S. Rao, Mechanical Vibrations, Pearson, 2005.

[20] J.S. Burdess, B. J. Gallacher et-al, The theory of a trapped degenerate mode resonator In Press Journal of the Acoustical Society of America, 2017.

[21] K.F. Graff, Wave Motion in Elastic Solids, Dover Publications, 1991

[22] S.M. Hu, Film edge induced stress in silicon substrates, Appl. Phys. Lett. 32, 5 (1978).

[23] C. Caliendo, M. Hamidullah, and F. Laidoudi , Amorphous SiC/c-ZnO-Based Quasi-Lamb Mode Sensor for Liquid Environments, Sensors (Basel). 2017 Jun; 17(6): 1209. doi: 10.3390/s17061209

.